

Computation of Transonic Diffuser Flows by a Lagged $k-\omega$ Turbulence Model

Q. Xiao* and H. M. Tsai†

National University of Singapore, Singapore 119260, Republic of Singapore
 and

F. Liu‡

University of California, Irvine, Irvine, California 92697-3975

The lag model proposed by Olsen and Coakley is applied in combination with the baseline $k-\omega$ two-equation turbulence model to simulate the steady and unsteady transonic flows in a diffuser. A fully implicit time-accurate multigrid algorithm is used to solve the unsteady Navier–Stokes equations and the coupled $k-\omega$ turbulence model equations. Two test cases are investigated, one with a weak shock in the channel corresponding to an exit-static-to-inlet-total pressure ratio $Rp=0.82$ and the other with a strong shock corresponding to $Rp=0.72$. Unsteady flows are induced by imposing fluctuating backpressure. Computational results are compared with experimental data and demonstrate notable improvement by the lag model for flows with strong shock–boundary-layer interactions.

Nomenclature

a	= sound speed
E	= total energy
e	= internal energy
f	= backpressure frequency
h	= channel height
k	= turbulent mixing energy
M	= Mach number
Pr_L, Pr_T	= laminar and turbulent Prandtl numbers
p	= pressure
Q	= source term of lag equation
Rp	= pressure ratio
$\mathbf{R}^*(\mathbf{W})$	= vector of the unsteady residuals
T	= temperature
t	= real time
t^*	= pseudotime
$\mathbf{u}_i, \mathbf{u}_j$	= velocity vector
\mathbf{W}	= vector of flow state variables
x	= streamwise coordinates, 0 at throat
y	= vertical coordinate, 0 at lower wall
y_w^+	= non dimensional distance from wall
β, β^*, σ	= turbulent closure coefficients
$\sigma^*, \varepsilon, \varepsilon^*$	
γ	= ratio of specific heats
δ_{ij}	= Kronecker delta function
μ, μ_t	= dynamic molecular viscosity and eddy viscosity
ν, ν_t	= kinematic molecular viscosity and eddy viscosity
ρ	= density
$\tau_{ij}, \hat{\tau}_{ij}$	= Reynolds and total stress tensors
ω	= specific dissipation rate

Subscripts

E	= equilibrium
th	= throat

w	= wall
1	= inlet
2	= exit

I. Introduction

ACCURATE prediction of unsteady flows is an important capability in the analysis and design of modern aircraft and the turbomachinery of gas-turbine engines. Major improvements in computing power and computational methods have resulted in the appearance of unsteady flow computations that employ Euler and Navier–Stokes equations. In spite of these recent advances, computation of unsteady flows with shock interaction remains a problem that demands large amounts of computational resources and improved accuracy in numerical discretization and turbulence modeling.

Significant progress has been made in the development of efficient numerical algorithms for time-accurate computations. Jameson¹ proposed an efficient multigrid-driven implicit approach to the solution of the Euler equations using the technique of dual time stepping. It uses an implicit multistep discretization in time. A large set of simultaneous nonlinear equations is formed and marched to steady state in pseudotime through a multigrid algorithm within each real time step. This approach has been used for aeroelastic studies and for unsteady flows in turbomachinery (Liu et al.² and Yao et al.³). Of note is that this method also facilitates the incorporation of turbulence models. Liu and Ji⁴ developed a fully implicit time-accurate multigrid algorithm to solve the coupled unsteady Navier–Stokes equations and the $k-\omega$ two-equation turbulence model equations. The scheme relaxes the Courant–Friedrichs–Lewy stability limit by using implicit time-accurate discretization. Local time stepping, residual smoothing, and multigrid techniques are used to accelerate the convergence for both the flow and the turbulence model equations.

The baseline $k-\omega$ two-equation turbulence model, as well as other classical one- or two-equation turbulence models, do not adequately account for “history” effects encountered in flows with large pressure gradients involving separation and shock waves, such as those found in nozzles and diffusers. The Reynolds stresses predicted by such models respond instantaneously to changes to the local strain rate. More complex Reynolds stress models address this problem due to builtin lagging of Reynolds stresses in both time and space in the model equations, but extensive studies show difficulties for their practical use. They are computationally more involved and numerically stiff and, hence, generally not practical for complex problems. Nonlinear algebraic Reynolds stress models

Received 2 August 2002; revision received 5 February 2003; accepted for publication 5 February 2003. Copyright © 2003 by the authors. Published by the American Institute of Aeronautics and Astronautics, Inc., with permission. Copies of this paper may be made for personal or internal use, on condition that the copier pay the \$10.00 per-copy fee to the Copyright Clearance Center, Inc., 222 Rosewood Drive, Danvers, MA 01923; include the code 0748-4658/03 \$10.00 in correspondence with the CCC.

*Research Scientist, Temasek Laboratories, Kent Ridge Crescent.

†Principal Research Scientist, Temasek Laboratories, Kent Ridge Crescent. Member AIAA.

‡Associate Professor, Department of Mechanical and Aerospace Engineering, Senior Member AIAA.

have emerged as a simpler alternative. However, it is known that such models also respond too rapidly to mean flow conditions as one- and two-equation models do. Olsen and Coakley⁵ recently proposed a new class of models, which is termed the lag model. The basic idea of the lag model is to take a baseline two-equation model and couple it with a third equation, the lag equation, to model the nonequilibrium effects for the eddy viscosity. Computations of steady incompressible and transonic flows by Olsen and Coakley show significant improvement by the lag model over the plain $k-\omega$ turbulence model. Its simplicity and computational efficiency is an added advantage, and thus, it serves as a convenient and effective enhancement to existing one- or two-equation turbulence models for three-dimensional flows.

The usefulness of this lag model is explored for steady and unsteady flow calculations with shock-boundary-layer interactions. A geometrically simple but computationally challenging problem is the unsteady flow due to fluctuating backpressure in a transonic diffuser. Bogar et al.,⁶ Salmon et al.,⁷ and Sajben et al.⁸ presented experimental measurements for the pressure field in a transonic and supersonic diffuser with an oscillating shock wave. Liou and Coakley⁹ numerically investigated this configuration using a modified McCormack's hybrid method for the unsteady Navier-Stokes equation and the $k-\omega^2$ turbulent model without the lag model. In this paper, calculations are conducted of the same test problem to assess the utility of the lag model for unsteady problems.

The lag model is here incorporated into the flow code developed by Liu and Ji⁴ to solve the coupled unsteady Navier-Stokes equations and the $k-\omega$ two-equation turbulence model equations by a fully implicit time-accurate multigrid method. In the following sections, the mathematical formulation of the Navier-Stokes and turbulence model equations and the numerical solution method are outlined. This is followed by the discussion of the computed numerical results for the flowfield. Conclusions are given in the final section.

II. Mathematical Formulation and Numerical Method

A. Governing Equations

The governing equations for the unsteady compressible turbulent flow with use of the Wilcox¹⁰ $k-\omega$ model and the lag model by Olsen and Coakley⁵ are expressed as follows.

Mass conservation:

$$\frac{\partial \rho}{\partial t} + \frac{\partial}{\partial x_j}(\rho u_j) = 0 \quad (1)$$

Momentum conservation:

$$\frac{\partial}{\partial t}(\rho u_i) + \frac{\partial}{\partial x_j}(\rho u_j u_i) = -\frac{\partial p}{\partial x_i} + \frac{\partial \hat{\tau}_{ji}}{\partial x_j} \quad (2)$$

Mean energy conservation:

$$\frac{\partial}{\partial t}(\rho E) + \frac{\partial}{\partial x_j}(\rho u_j H) = \frac{\partial}{\partial x_j} \left[u_i \hat{\tau}_{ij} + (\mu + \sigma^* \mu_T) \frac{\partial k}{\partial x_j} - q_j \right] \quad (3)$$

Turbulent mixing energy:

$$\frac{\partial}{\partial t}(\rho k) + \frac{\partial}{\partial x_j}(\rho u_j k) = \tau_{ij} \frac{\partial u_i}{\partial x_j} - \beta^* \rho \omega k + \frac{\partial}{\partial x_j} \left[(\mu + \sigma^* \mu_T) \frac{\partial k}{\partial x_j} \right] \quad (4)$$

Specific dissipation rate:

$$\begin{aligned} \frac{\partial}{\partial t}(\rho \omega) + \frac{\partial}{\partial x_j}(\rho u_j \omega) &= \left(\frac{\varepsilon \omega}{k} \right) \tau_{ij} \frac{\partial u_i}{\partial x_j} \\ &- \beta \rho \omega^2 + \frac{\partial}{\partial x_j} \left[(\mu + \sigma \mu_T) \frac{\partial \omega}{\partial x_j} \right] \end{aligned} \quad (5)$$

Turbulent eddy viscosity:

$$\frac{\partial}{\partial t}(\rho v_i) + \frac{\partial}{\partial x_j}(\rho u_j v_i) = a(R_T) \omega \rho (v_{iE} - v_i) \quad (6)$$

The total energy and enthalpy are $E = e + k + \mathbf{u}_i \mathbf{u}_i / 2$ and $H = h + k + \mathbf{u}_i \mathbf{u}_i / 2$, respectively, with $h = e + p / \rho$ and $e = p / [(\gamma - 1)\rho]$. Other quantities are defined in the following equations:

$$\mu_T = \rho v_i \quad (7)$$

$$v_{iE} = \frac{\varepsilon^* k}{\omega} \quad (8)$$

$$R_T = \frac{\rho k}{\mu \omega} \quad (9)$$

$$S_{ij} = \frac{1}{2} \left(\frac{\partial u_i}{\partial x_j} + \frac{\partial u_j}{\partial x_i} \right) \quad (10)$$

$$\tau_{ij} = 2\mu_T \left(S_{ij} - \frac{1}{3} \frac{\partial u_k}{\partial x_k} \delta_{ij} \right) - \frac{2}{3} \rho k \delta_{ij} \quad (11)$$

$$\hat{\tau}_{ij} = 2\mu \left(S_{ij} - \frac{1}{3} \frac{\partial u_k}{\partial x_k} \delta_{ij} \right) + \tau_{ij} \quad (12)$$

$$q_j = - \left(\frac{\mu}{Pr_L} + \frac{\mu_T}{Pr_T} \right) \frac{\partial h}{\partial x_j} \quad (13)$$

$$a(R_T) = a_0 \left[\frac{(R_T + R_{T0})}{(R_T + R_{T\infty})} \right] \quad (14)$$

The closure constants used in the preceding equations are $a_0 = 0.35$, $R_{T0} = 1$, $R_{T\infty} = 0.01$, $\varepsilon = \frac{5}{9}$, $\varepsilon^* = 1$, $\beta = 0.075$, $\beta^* = 0.09$, $\sigma = 0.5$, and $\sigma^* = 0.5$.

B. Lag Model

As pointed out by Olsen and Coakley,⁵ conventional one- and two-equation turbulence models generate Reynolds stresses that respond too rapidly to changes in mean flow conditions partially due to the need to reproduce accurately equilibrium flows. As a result, these baseline turbulence models give unsatisfactory results for flows with significant separation under adverse pressure gradients or across shock waves. In the preceding formulation [Eqs. (1–14)], the standard $k-\omega$ turbulent model [Eqs. (4) and (5)] is kept unchanged. However, the k and ω are only used to predict the equilibrium eddy viscosity v_{iE} . An additional equation [Eq. (6)] is used to predict the actual eddy viscosity v_i . This lag equation is essentially a relaxation model intended to account for memory effects of the turbulence eddy viscosity in adjusting to its local equilibrium value. The left-hand side of Eq. (6) is simply the Lagrangian derivative of v_i , which is driven on the right-hand side by its deviation from the equilibrium turbulence eddy viscosity v_{iE} predicted by the conventional k and ω model. The coefficient $1/[a(R_T)\omega]$ is the timescale for this nonequilibrium process. The function given by Eq. (14) with the prescribed constants given earlier ensures a large relaxation time constant, that is, a large time delay, when $R_T = \mu_{iE}/\mu$ is large. This is also the case when ω becomes small. On the other hand, it is shown by Olsen and Coakley⁵ that Eq. (6) is decoupled from the k and ω equations for such equilibrium turbulence flows such as the decay of isotropic homogeneous turbulence and fully developed channel flows. In the case of fully developed channel flows, the lag model predicts the desired equilibrium value: $v_i = v_{iE}$.

Notice that Eq. (6) involves only a simple inviscid transport operator and a source term. It does not involve any diffusion terms nor any wall distances as are needed by the Spalart-Allmaras one-equation model¹¹ or by the Shear-Stress-Transport (SST) $k-\omega$ model.¹² Consequently, its numerical solution is rather benign and can be easily coupled with the Navier-Stokes and the $k-\omega$ equations in a time-marching method.

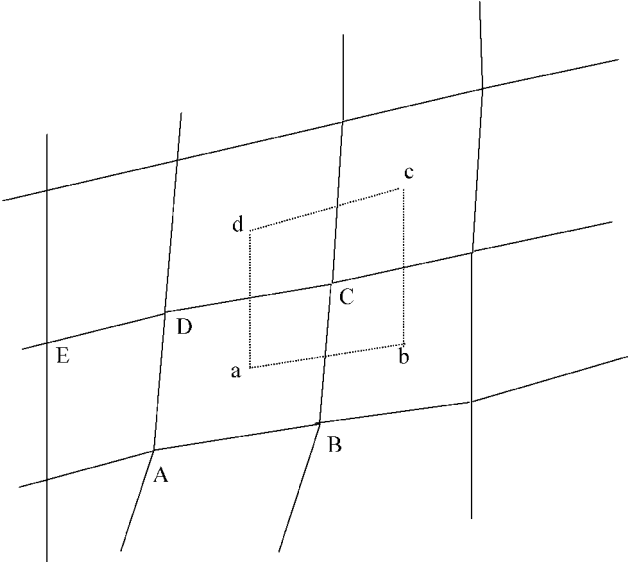


Fig. 1 Control volume.

C. Numerical Method

The basic numerical method used to solve the preceding system of equations follows that described in detail in Refs. 4 and 13. The integral forms of the conservation equations are discretized on quadrilateral cells using the finite volume approach. A staggered scheme is used for the coupling of Navier–Stokes equations and the k – ω and lag equations, that is, the flow variables ρ , ρu_i , and ρE are defined at the cell centers (a–d in Fig. 1), whereas turbulent variables ρk , $\rho \omega$, and ρv_i are stored at the cell vertex (A–D in Fig. 1).

After applying the governing Eqs. (1–6) to each cell in the mesh, we obtain a set of ordinary differential equations of the form

$$\frac{d}{dt}(\mathbf{W}_{ij} V_{ij}) + \mathbf{R}(\mathbf{W}_{ij}) = 0 \quad (15)$$

where $\mathbf{W} = [\rho, \rho u_i, \rho E, \rho k, \rho \omega, \rho v_i]^T$, V_{ij} is the volume of the i, j cell, and $\mathbf{R}(\mathbf{W}_{ij})$ is the residual that is obtained by evaluating the flux integral in Eqs. (1–6). A central difference scheme is used to discretize the diffusive terms in the Navier–Stokes and the k – ω equations. For the convective terms, a second-order MUSCL-type upwind biased scheme using Roe’s flux-differencesplitting method is used in the Navier–Stokes equations, and a second-order flux-splitting scheme based on the convective velocities is applied in the k – ω and lag equations. (See Refs. 4 and 13 for details.) For example, if the calculated normal convective velocity on the cell face ad is positive (Fig. 1), a second-order upwind interpolation for ρv_i at the cell face is $\rho v_i = 0.5 \times [3(\rho v_i)_D - (\rho v_i)_E]$.

The dual time-stepping method proposed by Jameson¹ is adopted here for the time discretization. The method uses an implicit physical time discretization. At each physical time step, the equations are integrated in a pseudotime to obtain the solution to the steady state in pseudotime. This method combines the advantage of both implicit methods and the fast solution techniques that have been developed for steady solutions (multigrid, implicit residual smoothing, etc.).

To obtain a fully implicit algorithm, Eq. (15) is approximated as follows:

$$\frac{d}{dt}(\mathbf{W}_{ij}^{n+1} V_{ij}^{n+1}) + \mathbf{R}(\mathbf{W}_{ij}^{n+1}) = 0 \quad (16)$$

where the superscript $n+1$ denotes the time level $(n+1)\Delta t$. The d/dt operator is approximated by an implicit backward difference formula. For a second-order accurate operator, Eq. (16) can be expressed in the following form:

$$(3/2\Delta t)[\mathbf{W}_{ij}^{n+1} V_{ij}^{n+1}] - (2/\Delta t)[\mathbf{W}_{ij}^n V_{ij}^n] + (1/2\Delta t)[\mathbf{W}_{ij}^{n-1} V_{ij}^{n-1}] + \mathbf{R}(\mathbf{W}_{ij}^{n+1}) = 0 \quad (17)$$

Equation (17) represents an implicit set of coupled ordinary differential equations. These equations can be solved at each time step using the same multistage technique for explicit steady-state calculations if we define the modified residual $\mathbf{R}^*(\mathbf{W})$ as

$$\mathbf{R}^*(\mathbf{W}) = \mathbf{R}(\mathbf{W}) + (3/2\Delta t)(\mathbf{W} V^{n+1}) - (2/\Delta t)(\mathbf{W} V^n) + (1/2\Delta t)(\mathbf{W} V^{n-1}) \quad (18)$$

and march to steady state in a fictitious time t^* with the following system of ordinary differential equations:

$$\frac{d\mathbf{W}}{dt^*} + \mathbf{R}^*(\mathbf{W}) = 0 \quad (19)$$

Within each real-time step, the set of ordinary differential equations (19) is solved using a five-stage Runge–Kutta scheme. To accelerate the convergence, the unsteady multigrid method proposed by Jameson¹ and further implemented by Liu and Ji⁴ is applied in the present study for all equations corresponding to Eqs. (1–6) in a coupled fashion.

Compared with other two-equation eddy-viscosity models such as the k – ε model, the k – ω model does not require damping functions in the viscous sublayer and, therefore, is mathematically simpler and less stiff near walls. However, the explicit time-marching formula for the k , ω , and lag equations within each stage of a multistage time-stepping scheme limits the time steps due to the nonlinear source terms in the k – ω and lag equations. The remedy used here is to treat parts of the source terms implicitly for the k – ω equations, which is demonstrated in detail in Refs. 4 and 13. For the lag equation, a similar implicit treatment of the source term is applied. The explicit scheme for Eq. (6) can be rewritten as

$$\frac{d(\mu_T)}{dt^*} + R^*(\mu_T) = 0 \quad (20)$$

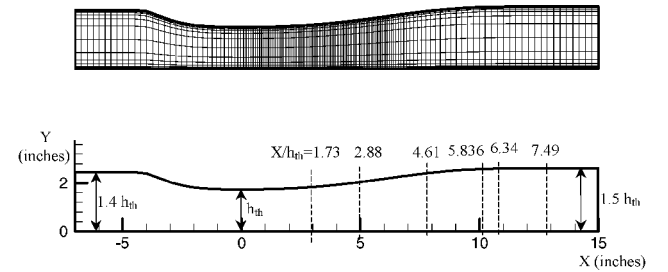


Fig. 2 Geometry and grid distribution, 321×65 mesh and $y_w^+ = 0.8$. (For clarity, grid is drawn by skipping one grid line in each direction.)

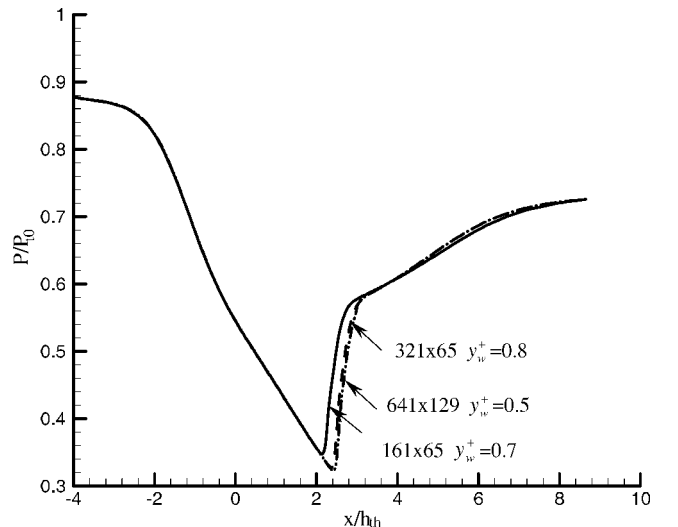


Fig. 3 Pressure distributions on the bottom wall (computed on different grids for the strong-shock case).

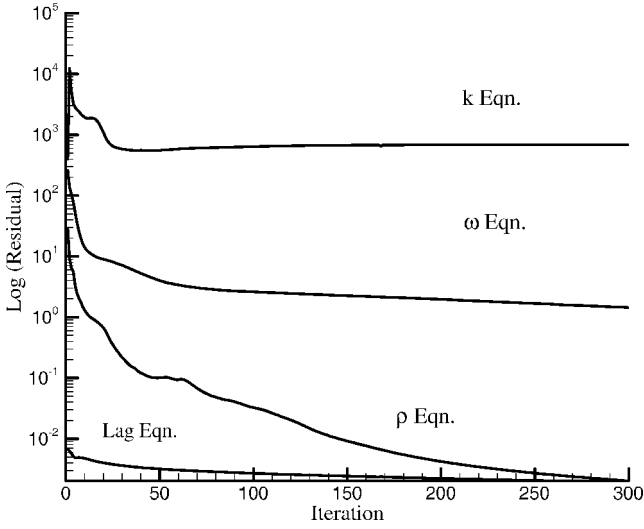
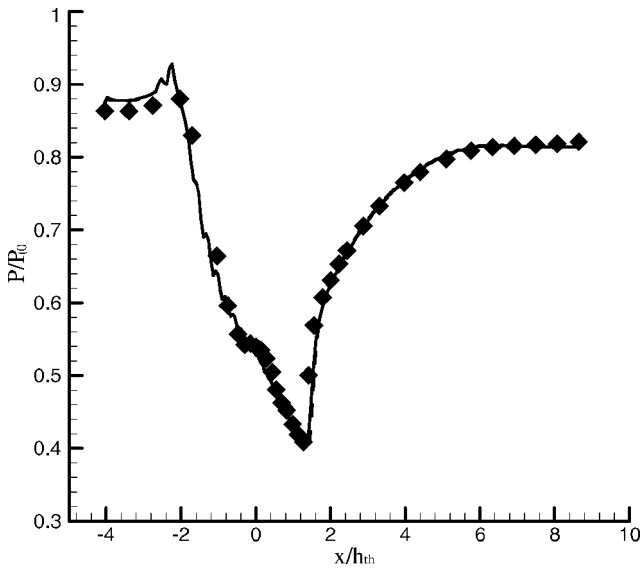
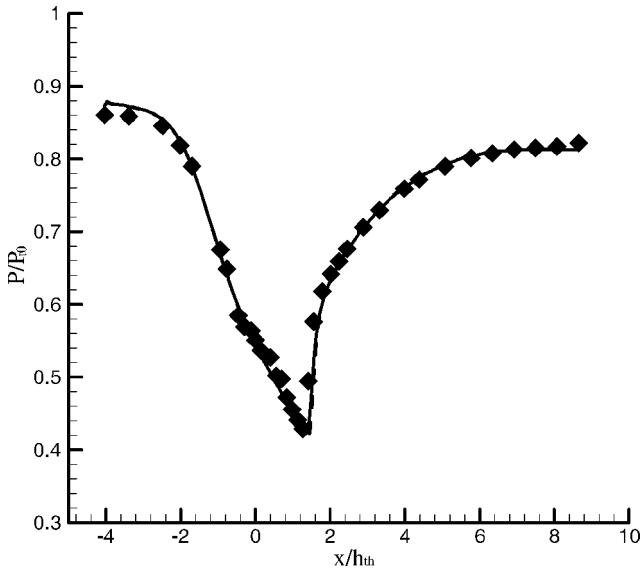


Fig. 4 Convergence history, 321×65 mesh and $y_w^+ = 0.8$.



a) Top wall



b) Bottom wall

Fig. 5 Pressure distributions along top and bottom walls, weak-shock case: \blacklozenge , experiment; ---, results without the lag model; and —, results with the lag model.

where $R^*(\mu_T)$ is the residual

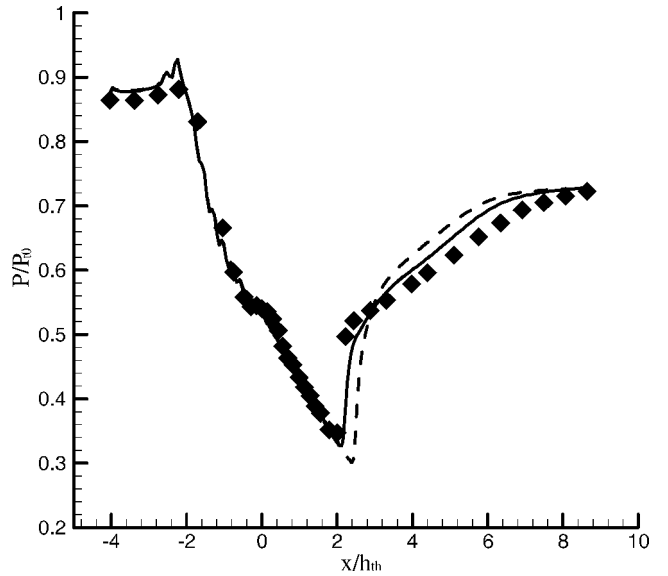
$$R^*(\mu_T) = \sum_{k=1}^{Nf} (F_c^n \Delta S)_K - Q_{\mu_t}^{n+1} \quad (21)$$

F_c^n is the convective flux and Q_{μ_t} the source term, which is made implicit by evaluating it at the new time level $(n + 1)$. To avoid solving nonlinear equations, it is linearized about the current time level n , resulting in

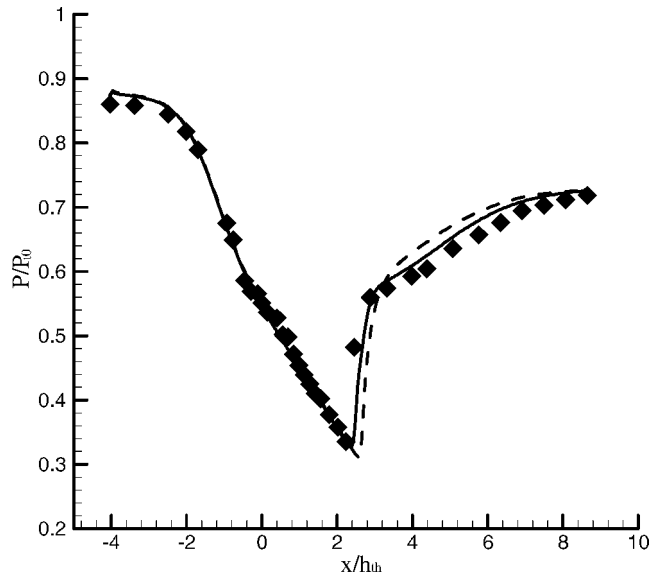
$$Q_{\mu_t}^{n+1} \approx Q_{\mu_t}^n + \frac{\partial Q_{\mu_t}}{\partial \mu_T} \Delta \mu_T^n = Q_{\mu_t}^n - a_0 \omega \left(\frac{\mu_{tE} + \mu_T}{\mu_{tE} + 0.01 \mu_T} \right) \Delta \mu_T^n \quad (22)$$

III. Results and Discussion

The numerical methods presented are applied to a two-dimensional steady and unsteady convergent/divergent diffuser investigated by Sajben et al.⁸ The bottom wall is flat and the geometry



a) Top wall



b) Bottom wall

Fig. 6 Pressure distributions along top and bottom walls, strong-shock case: \blacklozenge , experiment; ---, results without the lag model; and —, results with the lag model.

of the upper wall is given by

$$\bar{h}(\bar{x}) = \frac{\alpha \cosh \zeta}{(\alpha - 1) + \cosh \zeta} \quad (23)$$

where

$$\zeta = \frac{C_1(\bar{x}/\bar{l})[1 + C_2(\bar{x}/\bar{l})]^{C_3}}{(1 - \bar{x}/\bar{l})^{C_4}} \quad (24)$$

the various constants for the top wall are given in Table 1. The height of the throat is $h_{th} = 1.7322$ in. (4.4 cm).

Table 1 Constants for channel height

Constant	Converging	Diverging
α	1.4114	1.5
\bar{l}	-2.598	7.216
C_1	0.81	2.25
C_2	1.0	0
C_3	0.5	0
C_4	0.6	0.6

The key parameter that characterizes this diffuser flow is the pressure ratio, $R_p = p_2/p_{t1}$, which is defined as the static pressure at the outlet p_2 divided by the inlet total pressure p_{t1} . The flow in the diffuser can be classified into the weak-shock and the strong-shock categories based on the pressure ratio. Two cases are investigated in the present work, one weak-shock case and one strong-shock case corresponding to $R_p = 0.82$ and 0.72 , respectively. The Reynolds number based on the channel width is 7×10^5 for both the strong-shock and the weak-shock cases. There is a shock-induced flow separation in the strong-shock case, whereas no flow separation occurs in the weak-shock case.

The boundary conditions are specified as follows.

At the inflow boundary, we set the experimental values of $p_{t1} = p_{t0} = 19.58$ psia, $T_{t1} = 500R$, and zero flow angles. Either the static pressure, the Mach number, or one Riemann invariant is extrapolated from inside the flowfield. The inlet values of ω is estimated as

$$\omega_1 = \mathcal{O}(10u_1/h) \quad (25)$$

where u_1 is the flow velocity at the inlet. The turbulent energy k_1 is specified with a small value to keep the inlet eddy viscosity at low

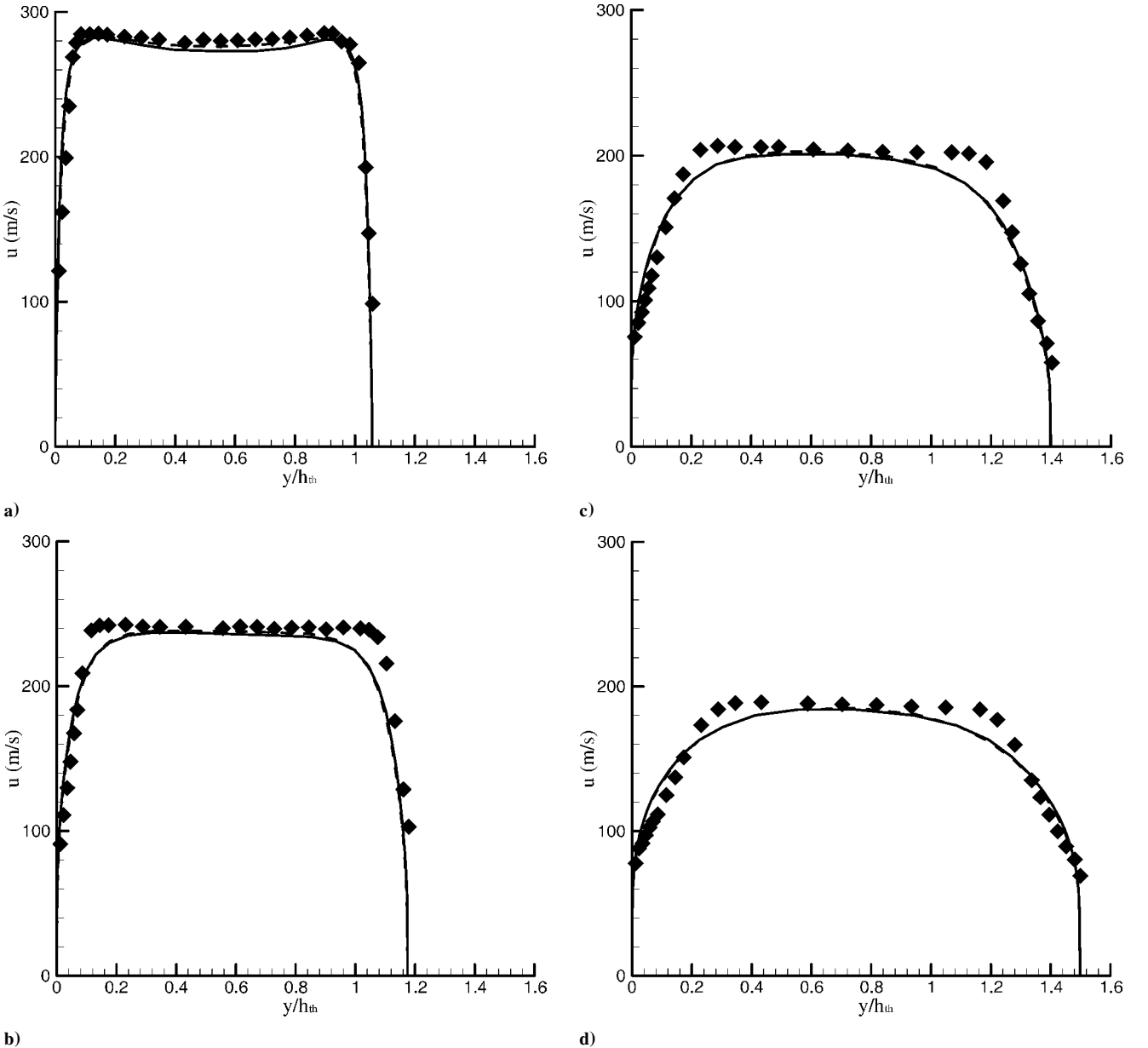


Fig. 7 Velocity profiles at different streamwise locations, weak-shock case: a) $x/h_{th} = 1.73$, b) $x/h_{th} = 2.88$, c) $x/h_{th} = 4.61$, and d) $x/h_{th} = 6.34$: \blacklozenge , experiment; ---, without the lag model; —, with the lag model.

level. For the diffuser calculations to be presented, the inlet ω and k_1 are taken as $\omega = 8$ and $k_1 = 1.5 \times 10^{-5}$. The eddy viscosity ν_t is set to ν_{tE} .

At the outflow boundary, only the static pressure is specified given that the experimental pressure ratio R_p and all of the other variables are extrapolated. To simulate the unsteady flow, a prescribed outlet static pressure taken from the experiment of Sajben et al.⁸ is imposed; $P_2 = P_e + P'_e \sin(2\pi ft)$, where P'_e is the amplitude of the oscillation, $P'_e/P_e = 0.011$, and f is the frequency. Only the case with $f = 75$ Hz is tested in the present study.

At the wall boundary, zero velocity is imposed, and the pressure is extrapolated to the wall. The turbulent mixing energy k is set to zero. The specific dissipation rate ω must satisfy the following asymptotic solution as the wall is approached:

$$\omega \rightarrow 6\nu_w / \beta y^2$$

as the distance $y \rightarrow 0$. In all of our numerical examples, the preceding equation is enforced only at the first grid point from the wall. The eddy viscosity ν_t is set to its equilibrium value ν_{tE} .

Figure 2 shows the geometry and grid distribution of a 321×65 grid used in the present study. Only every other grid line is plotted for clarity. The grid is generated algebraically. It consists of lines perpendicular to the x axis and clustering near the throat ($x = 0$). In the y direction, the mesh is stretched geometrically. The same grid spacing away from the wall is used on both the top and bottom walls, with the same geometric-progression ratio. At least one grid point near the wall is in the range of $y_w^+ < 1$. Three sets of grids are investigated herein for the grid resolution study: a 161×65 grid with maximum y_w^+ values next to the wall $y_w^+ = 0.7$, a 321×65 grid with $y_w^+ = 0.8$, and a 641×129 grid with $y_w^+ = 0.5$. The computed streamwise pressure distributions along the bottom wall for the steady strong-shock case are shown in Fig. 3. No significant differences exist between the solution on the 321×65 grid with $y_w^+ = 0.8$ and that on the 641×129 grid with $y_w^+ = 0.5$. Therefore, the computational results presented are conducted on the grid 321×65 with $y_w^+ = 0.8$.

The convergence history for the steady strong-shock case using a 321×65 mesh with $y_w^+ = 0.8$ is shown in Fig. 4 for the residuals of the k , ω , mass equations, and lag equations. Within 300 iterations, the residuals of the k , ω , and μ_T equations are reduced by 1 order

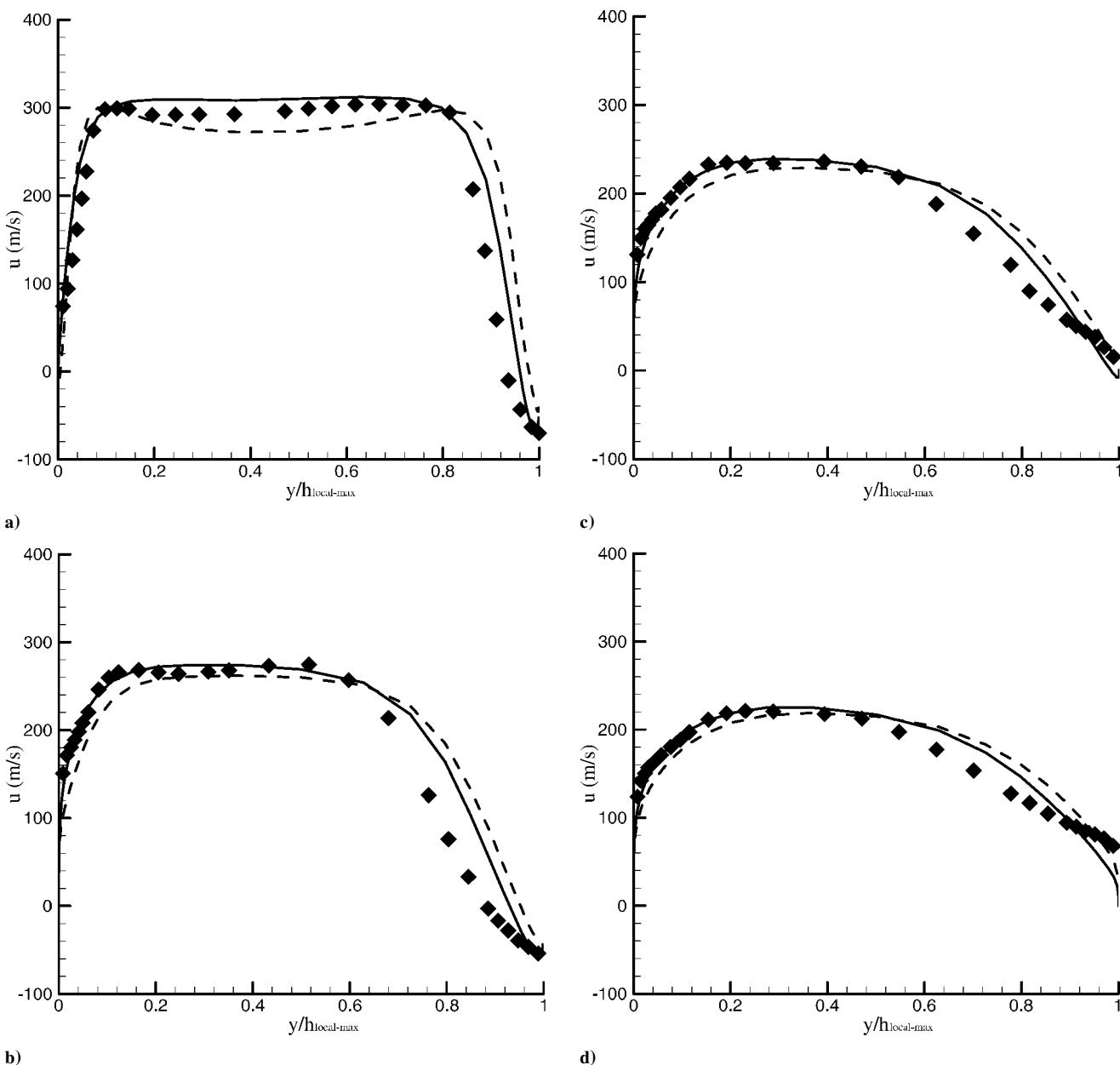


Fig. 8 Velocity profiles at different streamwise locations, strong-shock case: a) $x/h_{th} = 2.88$, b) $x/h_{th} = 4.61$, c) $x/h_{th} = 6.34$, and d) $x/h_{th} = 7.49$: \blacklozenge , experiment; ---, without the lag model; and —, with the lag model.

of magnitude, whereas the residual of the mass equation is reduced by 3–4 orders of magnitude.

The time needed for the steady case on a 321×65 grid with 300 iterations is about 30 min on a personal computer workstation with an Intel PIII 1.0-GHz processor and 1-GB RAM. For the unsteady calculation, it takes about 240 s to complete 40 multigrid cycles within one real-time step on a 321×65 mesh, corresponding to a time of 2.4 h for one period computation with 36 real-time steps.

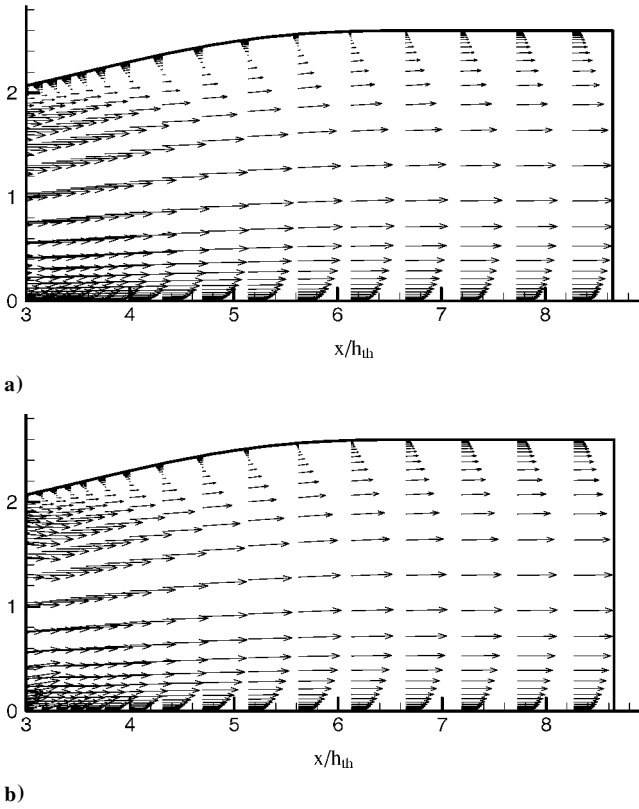


Fig. 9 Velocity vector in the separation region for the strong-shock case: a) with the lag model and b) without the lag model.

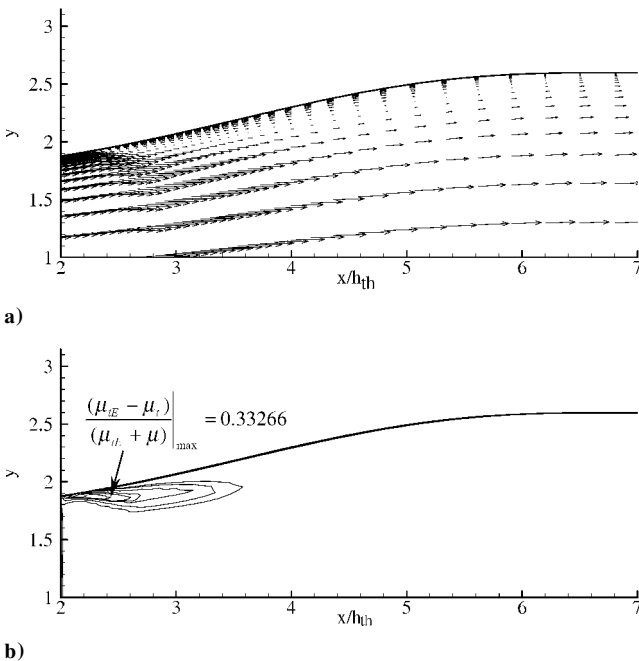


Fig. 10 Velocity vector and $(\mu_E - \mu_t)/(\mu_E + \mu)$ contour in the range $2.0 < x/h_{th} < 7.0$, $1.0 < y < 1.79$, strong shock case: a) velocity vector and b) $(\mu_E - \mu_t)/(\mu_E + \mu)$ contour, maximum value = 0.333, minimum value = 0.089, and interval = 0.0488.

Steady Case

Figures 5a and 5b show the pressure distributions on the top and bottom walls for the steady weak-shock case. For comparison, the experimental results of Sabjen et al.⁸ are also included. No significant differences are observed between the results obtained with and without the lag model. This fact implies that the lag model has no effect on the pressure distribution for the weak-shock case. The results of the strong-shock case are shown in Figs. 6a and 6b. Both Figs. 6a and 6b show that the results with the lag model are closer to the experimental data than the corresponding results without the lag model.

The velocity profiles at different streamwise locations for the weak-shock and the strong-shock cases are shown in Figs. 7a–7d and 8a–8d, respectively, where $h_{local-max}$ is the channel width at different streamwise locations, along with the experimental data from Sabjen et al.⁸ (The locations corresponding to the different values of x/h_{th} are marked in Fig. 2.) For the weak-shock case, the computational results agree reasonably well with the experimental data. The differences between the results with and without the lag model are small. The results for the strong-shock case do not show

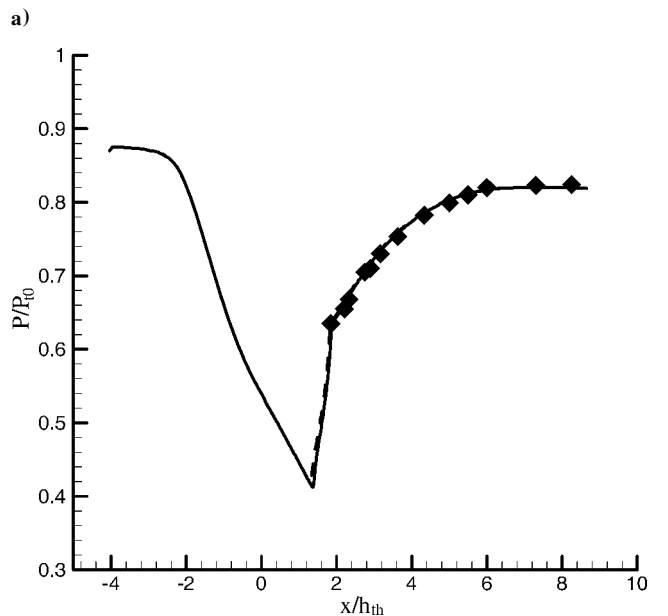
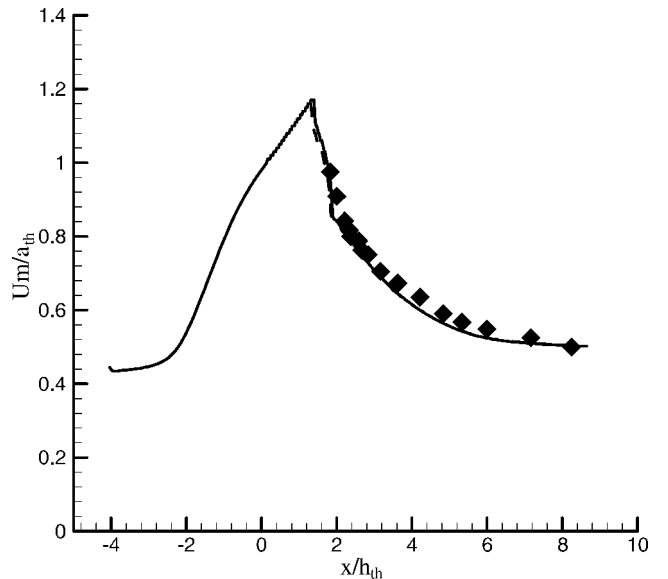


Fig. 11 Distributions of midstream time-mean velocity and pressure, weak-shock case: a) velocity and b) pressure: \blacklozenge , experiment; ---, without the lag model; —, with the lag model.

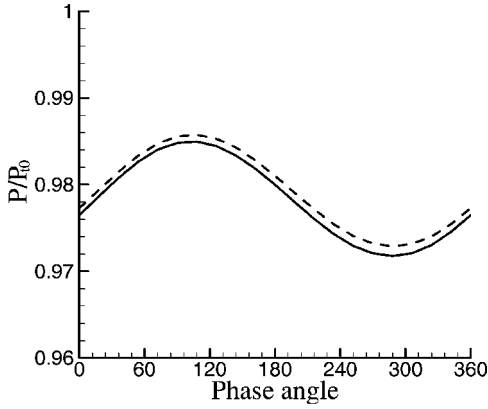
as good agreement with the experimental data as those for the weak-shock case. However, the computation with the lag model yields a noticeable improvement over that without the lag model for this strong shock case.

The major difference between the weak-shock and the strong-shock cases is the existence of a shock-induced separation in the strong-shock case. The computational results show that the separation bubble on the top wall extends to about $x/h_{th} = 6$ for the strong-shock case, whereas no separation is observed for the weak-shock case. The effect of the lag model on the prediction of flow separation is shown in Figs. 9a and 9b for the strong-shock case. (For clarity, the vectors are shown by skipping four lines in the stream/wise direction and two grid lines in the y direction.) The results obtained by the lag model show a slightly larger flow separation region than the corresponding results without the lag model.

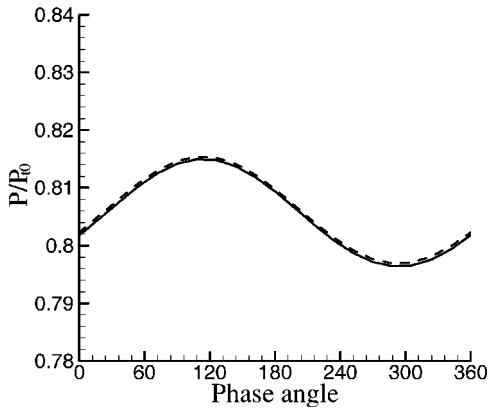
Comparisons of the computed separation and reattachment points and separation lengths with the experimental data and two computational results by the WIND computer code presented in Georgiadis et al.¹⁴ are listed in Table 2. They are WIND $k-\epsilon$ without correction and WIND $k-\epsilon$ with two correction factors. The first correction factor is the Sarkar compressibility correction, which provides for an increase in the dissipation rate at higher Mach numbers. Another correction factor is the variable C_μ option, which reduces the turbulent

Table 2 Comparison of flow separation (steady strong shock)

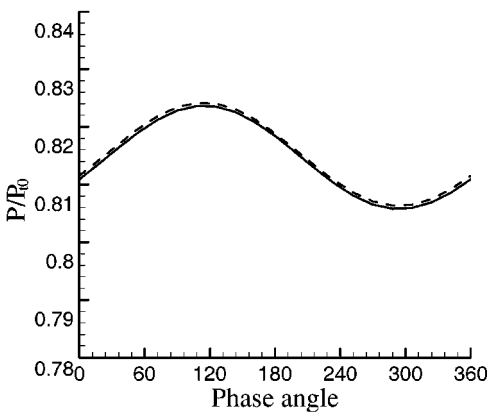
Experiment/ computational methods	Separation location x/h_{th}	Reattachment location x/h_{th}	Separation length $\Delta x/h_{th}$
Experiment	1.98	6.00	4.02
WIND $k-\epsilon$ (no correction)	2.5	4.59	2.09
WIND $k-\epsilon$ (Sankar and variable C_μ)	2.2	5.96	3.76
WIND SST	2.0	6.79	4.79
Normal $k-\omega$	2.65	5.93	3.28
$k-\omega$ plus lag model	2.29	6.32	4.03



a)

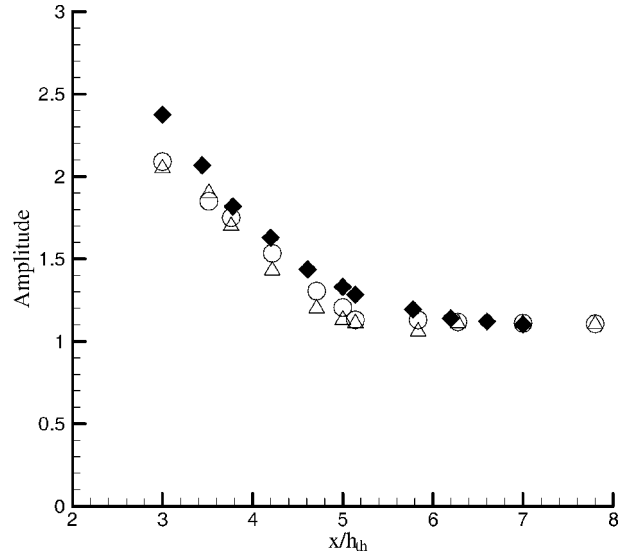


b)

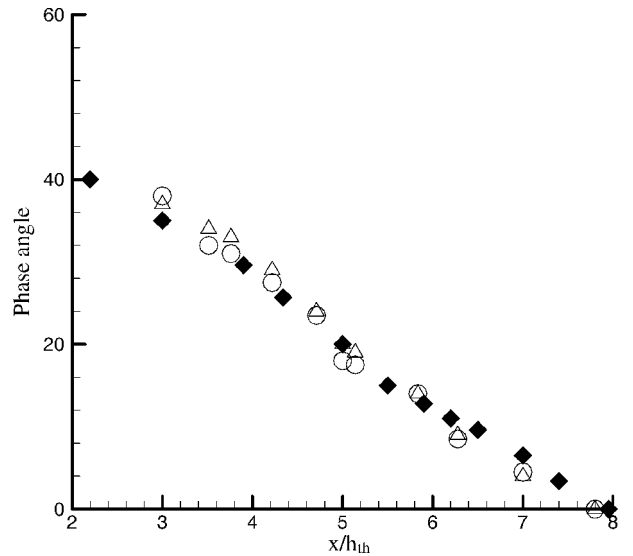


c)

Fig. 12 Variations of midstream total pressure and static pressure and top wall pressure within one period at $x/h_{th} = 5.836$: a) midstream total pressure, b) midstream static pressure, and c) top wall pressure: —, with the lag model and ---, without the lag model.



a)



b)

Fig. 13 Distributions of amplitude and phase angle of midstream pressure, weak-shock case: a) amplitude and b) phase angle: ♦, experiment; ○, with the lag model; and △, without the lag model.

viscosity in regions where the ratio of production-to-dissipation of turbulent kinetic energy becomes large.

The comparison reveals that the separation length and separation location obtained with the lag model is closer to the experimental data than the corresponding results without the lag model. However, it seems that the location of reattachment predicted by the lag model shifts slightly downstream compared to the experimental results. The lag model also predicts a more accurate separation length than the WIND $k-\epsilon$ model with or without the two correction factors. The separation and reattachment locations obtained by the present lag model are better than those obtained by the WIND $k-\epsilon$ without the correction factors, but worse than those with the two correction factors. The WIND SST model results are also included in Table 1. It shows good agreement with the separation location, but the separation length is overpredicted. The present computation with the lag model yields the best overall result among the methods listed in Table 2.

Flow history information in a turbulence model significantly influences the accuracy of a computation for separated flows. This history effect is partially taken into account in a general two-equation turbulent model such as the $k-\omega$ model. However, it is found that turbulence adjusts to equilibrium on a timescale much slower than that for the change of the mean strain-tensor estimated by the normal two-equation models. The principal effect of the lag model is to reduce the Reynolds stress from the equilibrium value v_{iE} to a nonequilibrium lagged value v_i . This is important for flows with separation that are out of equilibrium. Figure 10 shows the contours of the relative deviation of the nonequilibrium eddy viscosity μ_{i1} from its equilibrium value μ_{iE} normalized by the total viscosity $(\mu_{iE} + \mu)$ for the strongshockcase. (For clarity, the vectors are shown by skipping four lines in the stream wise direction in Fig. 10a) The

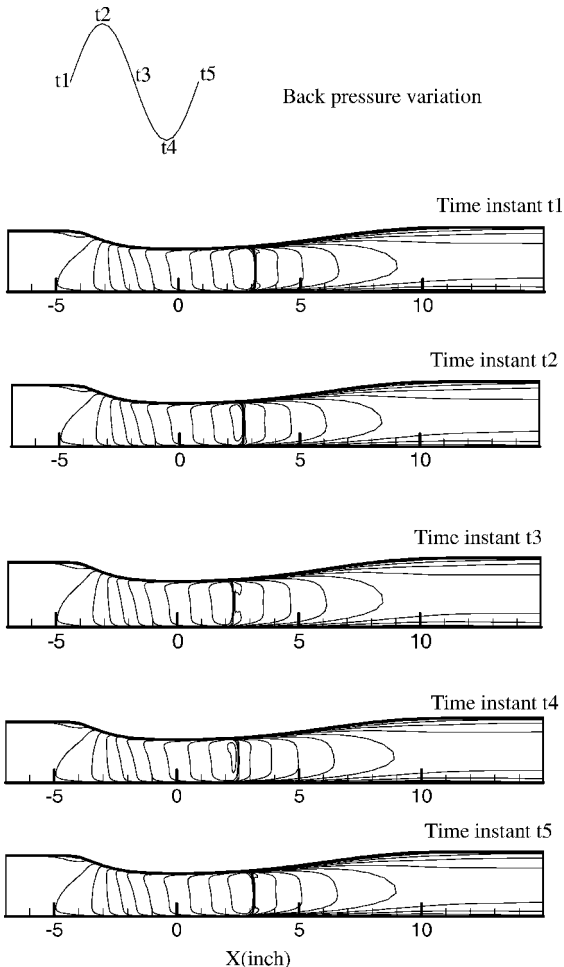


Fig. 14 Movement of shock location at different time instants within one period.

value of $(\mu_{iE} - \mu_{i1})/(\mu_{iE} + \mu)$ reaches a maximum of over 30% in the strong shock-induced separation region, indicating significant nonequilibrium effect.

Unsteady Case

The calculation of unsteady flow starts from a steady solution; the final flowfield becomes periodic forced by the oscillatory pressure ratio Rp . For the weak-shock case, the flow becomes periodic after 2–3 periods, whereas for the strong-shock case, 5–6 cycles are needed to achieve a fully developed periodic flow. Within each implicit time step, 30–40 multigrid cycles are used. Four levels of multigrid are used for accelerating the solution convergence.

Flow with a Weak Shock

Figures 11a and 11b show the computed streamwise distributions of the time-mean velocity and pressure in the midstream of the diffuser for the weak-shock case. The velocity is nondimensionalized by the sound speed at the throat, a_{th} . The experimental results are also included for comparison. The computational results are in good

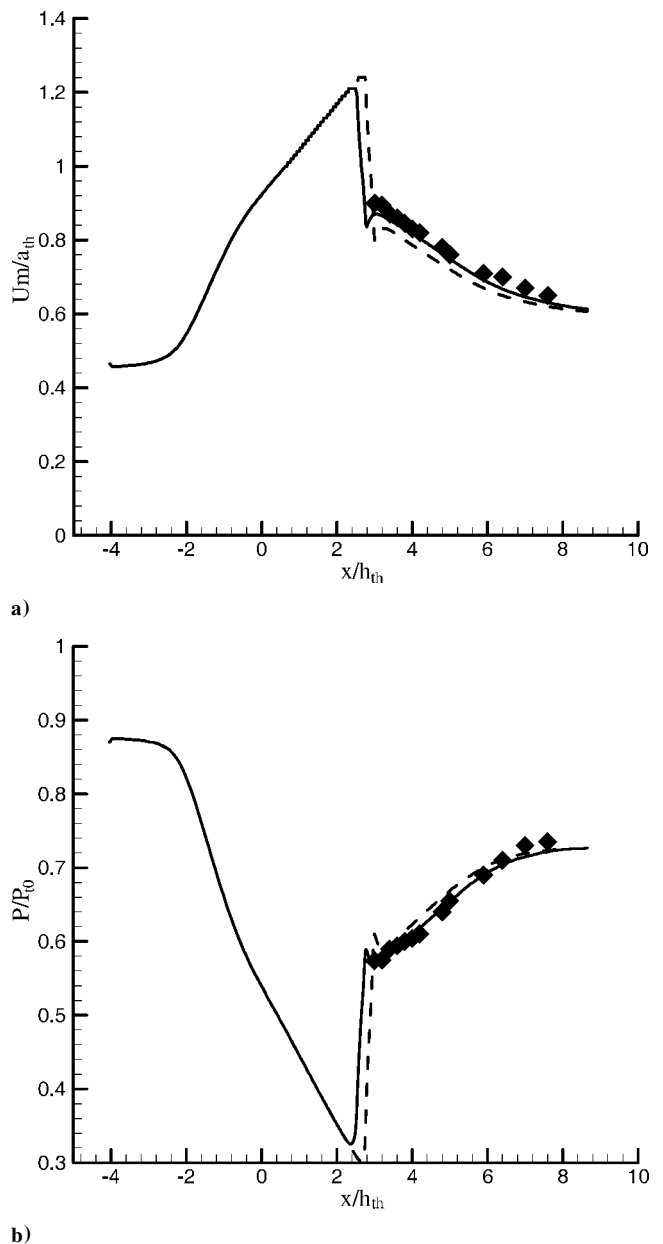


Fig. 15 Distributions of midstream time-mean velocity and pressure, strong-shock case: a) velocity and b) pressure: \blacklozenge , experiment; ---, without the lag model; and —, with the lag model.

agreement with the experimental data. In addition, no apparent differences between the results with and without the lag model can be observed from Figs. 11a and 11b. This fact implies that, for this unsteady weak-shock case, the effect of the lag model on the time-mean values is not significant. This resembles the conclusion found in the steady weak-shock case.

The variations of the unsteady total pressure and the static pressure at midstream and the static pressure on the top wall, all at $x/h_{th} = 5.836$ (refer to Fig. 2), are shown in Figs. 12a–12c within one oscillation cycle. The results show that all pressure oscillations nearly follow a sinusoidal form, similar to that of the imposed backpressure. Moreover, the differences between the results with and without the lag model are negligible. Figures 13a and 13b show the amplitude and phase angle distributions along the streamwise direction for the midstream pressure. The amplitude is normalized here

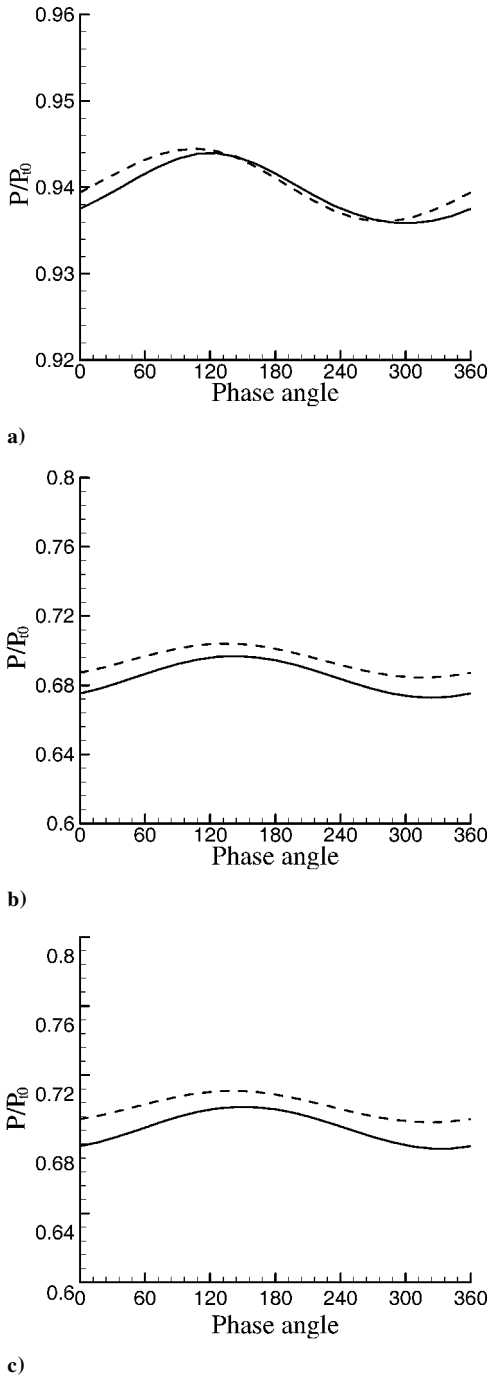


Fig. 16 Variations of midstream static and total pressure and top wall pressure within one period at $x/h_{th} = 5.836$, strong-shock case: a) midstream total pressure, b) midstream static pressure, and c) top wall pressure: —, with the lag model and - - -, without the lag model.

by the amplitude of the backpressure. The computational results are generally in agreement with the experimental results. No apparent effect of the lag model can be observed for this weak-shock case. The movement of shock location at different time instants within one period is shown in Fig. 14. The shock moves upstream and downstream with the backpressure fluctuation. It can be concluded from the results that the lag model has almost no effect on the computational results for the weak-shock case in which there is no flow separation.

Flow with a Strong Shock

The computational time-mean streamwise velocity and pressure distributions for the case with $Rp = 0.72$ are shown in Figs. 15a and 15b, as well as the experimental results. In contrast to the weak-shock case, the computational results by use of the lag model are closer to the experimental data for this case. This demonstrates that the lag model, which is effective for predicting separated flow, yields an improvement on the calculation.

Figures 16a–16c show the variations of total and static pressures at midstream and the pressure on the top wall at $x/h_{th} = 5.836$ within one oscillation cycle. In contrast to the results of the weak-shock

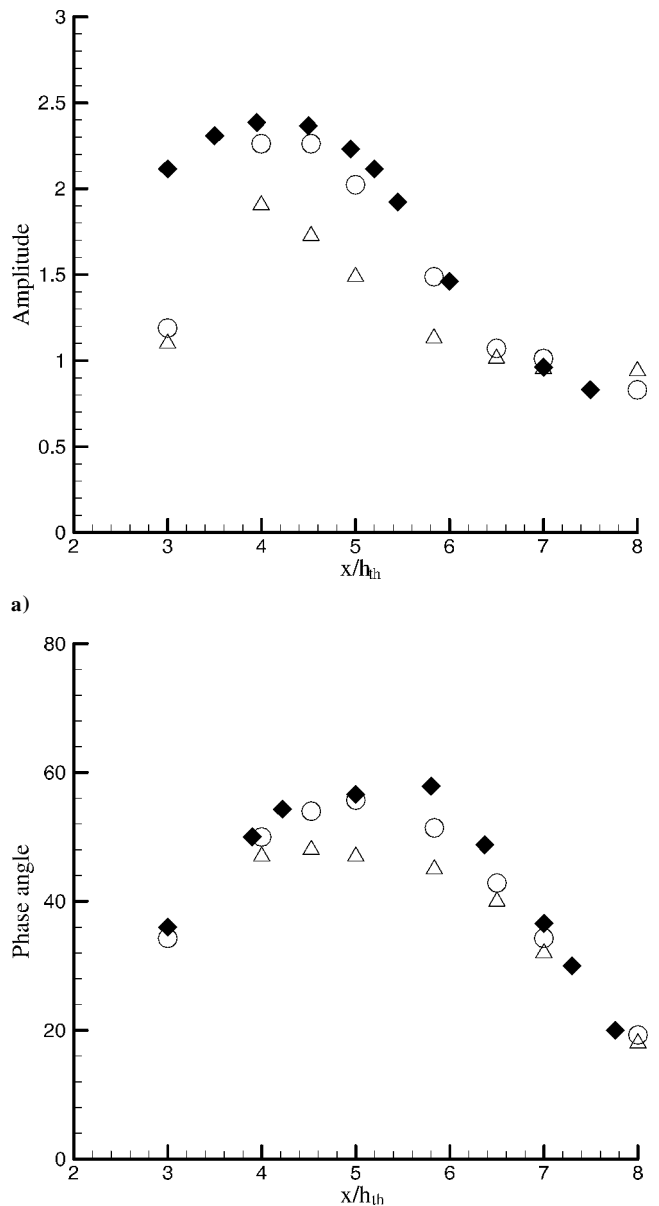


Fig. 17 Distributions of amplitude and phase angle of midstream pressure, strong-shock case: a) amplitude and b) phase angle: ♦, experiment; ○, with the lag model; and △, without the lag model.

case shown in Figs. 12a–12c, the differences in pressure with and without the lag model can be clearly seen. The streamwise distributions of amplitude and phase angle of the midstream pressure for the strong-shock case are shown in Figs. 17a and 17b, along with the experimental data. Compared to the weak-shock case, the amplitude and phase angle of the time-dependent midstream pressure are no longer monotonically decreasing with the streamwise distance (x/h_{th}) as the weak-shock results do. Here, they initially increase and then decrease with x/h_{th} after reaching their maximum values. Figures 17a and 17b show significant improvements by use of the lag model.

IV. Conclusions

The lag model in combination with the baseline $k-\omega$ turbulent model is applied to simulate the two-dimensional steady and unsteady convergent/divergent transonic diffuser flows using a multigrid finite volume method. For the unsteady flow, the dual-time approach is used to achieve time accuracy with a second-order implicit time-stepping method for both the Navier–Stokes and the turbulence model equations including the lag equation. Two flow cases are studied, one with a weak-shock wave and the other with a strong-shock wave. Results are presented and compared with experimental data and solutions obtained by other methods. The main conclusions can be summarized as follows.

1) For flows with little nonequilibrium effects, the lag model effectively reduces to the baseline $k-\omega$ model. No significant differences between the results with and without the lag model are observed for the weak-shock case studied in this paper.

2) Notably improved results are observed by using the lag model for the strong-shock case, in which there is flow separation, for both steady and unsteady situations. For the steady case, the predicted separation length is remarkably more accurate than that without the lag modification and predictions by several other two-equation models in the validation suite presented by Georgiadis et al.¹⁴ For the unsteady case, predictions of both the magnitude and the phase of the unsteady pressure along the diffuser agree significantly better with experimental data than those without the lag model.

3) The addition of the lag model does not pose extra numerical difficulties to existing time-marching codes. The lag model offers a convenient and effective way to augment existing baseline one- and

two-equation turbulence models by providing a relaxation mechanism for the turbulence eddy viscosity to adjust to its local equilibrium values. This nonequilibrium effect is important for flows with separation and shock–boundary-layer interaction problems.

References

- ¹Jameson, A., “Time Dependent Calculations Using Multigrid, with Applications to Unsteady Flows Past Airfoils and Wings,” AIAA Paper 91-1596, June 1991.
- ²Liu, F., Cai, J., Zhu, Y., Wong, A. S. W., and Tsai, H. M., “Calculation of Wing Flutter by a Coupled Fluid-Structure Method,” *Journal of Aircraft*, Vol. 38, No. 2, 2001, pp. 334–342.
- ³Yao, J., Jameson, A., Alonso, J. J., and Liu, F., “Development and Validation of a Massively Parallel Flow Solver for Turbomachinery Flows,” *Journal of Propulsion and Power*, Vol. 17, No. 3, 2001, pp. 659–668.
- ⁴Liu, F., and Ji, S., “Unsteady Flow Calculations with a Multigrid Navier–Stokes Method,” *AIAA Journal*, Vol. 34, No. 10, 1996, pp. 2047–2053.
- ⁵Olsen, M. E., and Coakley, T. J., “The Lag Model, a Turbulence Model for Non-equilibrium Flows,” AIAA Paper 2001-2564, June 2001.
- ⁶Bogar, T. J., Sajben, M., and Kroutil, J. C., “Characteristic Frequencies of Transonic Diffuser Flow Oscillations,” *AIAA Journal*, Vol. 21, No. 9, 1983, pp. 1232–1240.
- ⁷Salmon, J. T., Bogar, T. J., and Sajben, M., “Laser Velocimeter Measurements in Unsteady, Separated, Transonic Diffuser Flows,” *AIAA Journal*, Vol. 21, No. 12, 1983, pp. 1690–1697.
- ⁸Sajben, M., Bogar, T. J., and Kroutil, J. C., “Forced Oscillation Experiments in Supercritical Diffuser Flows,” *AIAA Journal*, Vol. 22, No. 4, 1984, pp. 465–474.
- ⁹Liou, M. S., and Coakley, T. J., “Numerical Simulations of Unsteady Transonic Flow in Diffusers,” *AIAA Journal*, Vol. 22, No. 8, 1984, pp. 1139–1145.
- ¹⁰Wilcox, D. C., “Reassessment of the Scale-Determining Equation for Advanced Turbulence Models,” *AIAA Journal*, Vol. 26, No. 11, 1988, pp. 1299–1310.
- ¹¹Spalart, P. R., and Allmaras, S. R., “A One-equation Turbulence Model for Aerodynamic Flows,” *La Recherche Aérospatiale*, Vol. 1, 1994, pp. 5–21.
- ¹²Menter, F., “Two-Equation Eddy-Viscosity Turbulence Models for Engineering Applications,” *AIAA Journal*, Vol. 32, No. 8, 1994, pp. 1598–1605.
- ¹³Liu, F., and Zheng, X., “A Strongly-Coupled Time-Marching Method for Solving the Navier–Stokes and $k-\omega$ Turbulence Model Equations with Multigrid,” *Journal of Computational Physics*, Vol. 128, Aug. 1996, pp. 289–300.
- ¹⁴Georgiadis, N. J., Drummond, J. E., and Leonard, B. P., “Evaluation of Turbulence Models in the PARC Code for Transonic Diffuser Flows,” NASA TM-106391, Jan. 1994.